Article

A Computational Fluid Dynamics-Based Study on the Effect of Bionic-Compound Recess Structures in Aerostatic Thrust Bearings

Fangjian Yuan [1,2], **Hang Xiu** [1,2,*], **Guohua Cao** [1,2], **Jingran Zhang** [1], **Bingshu Chen** [1], **Yutang Wang** [3] **and Xu Zhou** [1]

1   College of Mechanical and Electric Engineering, Changchun University of Science and Technology, Changchun 130022, China; 18334943540@163.com (F.Y.); caogh@cust.edu.cn (G.C.); zhangjingran@cust.edu.cn (J.Z.); bingshuc2003@163.com (B.C.); 18804460095@163.com (X.Z.)
2   Chongqing Research Institute, Changchun University of Science and Technology, Chongqing 404100, China
3   Changchun Institute of Optics, Fine Mechanics and Physics, Chinese Academy of Sciences, Changchun 130033, China; ytwang@ciomp.ac.cn
*   Correspondence: xiuhang@cust.edu.cn

Abstract: To investigate the effect of recess structures on the static and dynamic performance of aerostatic thrust bearings and to explore superior designs, this study analyzes the load-capacity theoretical model, identifying that the throttling effect and pressure-holding effect of the recess are the key factors determining the bearings' static performance. Computational fluid dynamics (CFD) was used to evaluate three types of recess structures: a simple-orifice recess (SOR), a rectangular-compound recess (RCR), and a bionic-compound recess (BCR). The results indicate that the BCR structure demonstrates efficient transmission performance by reducing flow resistance and diverting air, while ensuring a reasonable pressure drop as the radial ratio α_i changes. Additionally, the smaller air capacity of the BCR structure contributes to enhanced bearing stability, showing clear advantages in both static and dynamic performance. This research illustrates the practical application of bionics in mechanical design and provides new theoretical foundations and design strategies for improving aerostatic bearing performance.

Keywords: aerostatic thrust bearing; bionics recess; CFD simulation; static and dynamic stability

1. Introduction

During the operation of aerostatic thrust bearings, air is continuously supplied from an external source, serving as a lubricant and replacing traditional rollers. This enables the bearings to be characterized by low noise, high precision, low friction, high speed and long service life, and they are widely used in aerospace, semiconductor processing and ultra-precision testing, among other applications [1,2]. Given the compressibility of air and the stringent requirements for precision, stability, and operational speed, the static performance of high-performance aerostatic thrust bearings—including load capacity, stiffness, and dynamic characteristics—has attracted significant attention from researchers and industry professionals [3]. Among various methods to enhance performance, recesses have emerged as particularly effective, leading to extensive investigation.

Hiromu Hashimoto et al. [4] optimized the design of grooves for thrust air bearings using a sequential quadratic programming method based on objective functions, including air-film thickness, bearing torque, air-film dynamic stiffness, and their combinations, with cubic spline functions representing the groove geometries. They found that the groove geometry optimizing air-film thickness or frictional moment was a helical groove, while the geometry optimizing dynamic stiffness was an improved helical groove. Tomotaka Yoshimura et al. [5] conducted a computational fluid analysis of airflow around the bearings,

comparing it with experimental photographs to investigate the cause of tiny fluctuations, termed nano-fluctuations, in the aerostatic thrust bearing confined by the T-shaped groove surface. Yinan Chen et al. [6] modeled four aerostatic bearings with grooves of different geometries by combining grooves with annular aerostatic thrust bearings featuring porous throttling. They investigated the pressure distribution, load-carrying capacity, stiffness, and flow characteristics of the flow field in the bearing gap through computational fluid dynamics simulations. Colombo, F et al. [7]. performed experimental and numerical simulations to analyze the effects of orifice diameter, position, and air supply pressure on the load capacity and air consumption of rectangular chambers. Puliang Yu et al. [8] designed a square microporous array restrictor for aerostatic bearings, revealing that the design effectively reduces turbulent vortices and micro-vibrations through numerical simulation and experimentation. Zhuang [9] examined bearing capacity and pressure distribution at varying eccentricities and design parameters using FDM modeling and CFD simulations. Gao et al. [10] explored the impact of six different chamber shapes on pressure distribution and load capacity at ultra-high speeds (200,000 rpm) through experimental and CFD analyses. Puliang Yu et al. [11] designed a novel primary and secondary orifice restrictor, and the static–dynamic characteristics based on this restrictor were investigated by using large eddy simulations and experiments. The results show that this type of restrictor can effectively suppress the generation of turbulent vortices. Qiao, Y.J. et al. [12] investigated the static performance of aerostatic bearings with trapezoidal groove restrictors and increased the bearing capacity by 18%. Mohamed E. Eleshaky [13] analyzed two structural forms of circular bearings using CFD simulations to investigate the mechanisms behind the pressure-drop phenomenon in aerostatic thrust bearings. Wenjun Li et al. [14] introduced a novel aerostatic bearing design featuring back-flow channels, which was validated through CFD and experimental studies. This new structure demonstrated improved load capacity, stiffness, and stability compared to traditional pocketed orifice-restricted aerostatic bearings. Siyu Gao et al. [15] examined the effects of various orifice length/diameter ratios (OLDR) on pressure, velocity, turbulence intensity, eddy currents, load capacity, stiffness, volumetric flow rate, and orifice flow resistance in aerostatic thrust bearings using computational fluid dynamics (CFD). The results indicated that the performance of aerostatic thrust bearings varied under different OLDRs. Ruzhong Yan [16] proposed six types of groove restrictor designs—linear, extended, S-shaped, elliptical, X-shaped, and mesh—for two common throttle arrangements (linear and rectangular) on the thrust surface. Numerical simulations of different bearing types revealed that the use of groove restrictors significantly enhances bearing capacity, static stiffness, operational accuracy, and longevity. Kai Feng [17] introduced an innovative restrictor structure for aerostatic bearings aimed at suppressing eddy currents by altering airflow characteristics within the groove. Both theoretical and experimental results indicated that the Arc Hole Bearing (AHB) achieved superior stability and the smallest vibration amplitude while maintaining consistent load capacity. In summary, numerous scholars have studied restrictors, focusing on various adjustments to structure parameters. These include optimizing the shapes of dynamic pressure grooves, refining groove designs through adjustments in dimensions and parameters, and altering the size specifications of the air supply orifice. Despite these advancements, there remains relatively limited research on directing fluid flow within bearings to optimize flow patterns and enhance both static and dynamic performance.

Biological structures, particularly vascular branching structures in plant leaves, have evolved to exhibit exceptional mass transfer capabilities in substance transport [18]. These branched networks have garnered attention across various fields, significantly enhancing humanity's ability to adapt to and transform nature while generating substantial economic benefits. For example, Ruofei Zhu [19] developed an artificial tree evaporator based on the Murray network, highlighting the value of branching structures in desalination applications. Guohui Zhou et al. [20] created a vapor chamber with a leaf-shaped liquid-absorbing core that promotes efficient condensate return for cooling. Shitong Chai [21] demonstrated that symmetric leaf-vein structures outperform their asymmetric counterparts in heat transfer

characteristics, emphasizing the potential of biomimetic design for optimizing fluid channel configurations in engineering applications. Yi Peng [22] designed a vapor-chamber wick structure inspired by the fractal architecture of leaf veins, featuring polygonal loops formed by Y-shaped bifurcations. This study demonstrated that the novel design outperforms parallel configurations in terms of permeability and resistance, highlighting its effectiveness in enhancing heat transfer and fluid transport efficiency. Xinyu Wan [23] investigated the flow field of a proton-exchange membrane fuel cell (PEMFC) by incorporating a Y-shaped tree-like fractal structure based on Murray's law. The research revealed that an optimal branching angle of 75° resulted in a 26.7% increase in maximum output power density compared to a parallel flow field, showcasing the advantages of tree-like fractal flow fields in improving transport characteristics and overall PEMFC performance. Chuangbei Ma [24] proposed a bio-inspired fractal microchannel heat sink with a modified secondary structure for efficient heat dissipation. The optimized design achieved a heat flux of 577 W/cm^2, demonstrating effectiveness in enhancing heat dissipation and reducing energy consumption. These findings illustrate the successful application of bionic structures in engineering and validate the potential of leaf vascular branching structures in fluid transport, offering new insights for designing recesses in air bearings.

Drawing on the functional similarities between leaf vascular branching structures and air diffusion processes in aerostatic thrust bearings, this study proposes a bionic-compound recess design. Simulations were conducted on three different types of recesses for aerostatic thrust bearings using CFD methods. A comparative analysis was performed between the bionic-compound recess and the other two structures, focusing on static and dynamic performance evaluation criteria. This study aims to explore this innovative design, elucidate the critical relationship between its performance and structure, and provide new insights for enhancing the performance of aerostatic bearings.

2. Compound Recess Based on the Bionic Concept

2.1. Bionic Recess Design

Certain structures in nature, such as leaf veins, animal lungs, and plant roots, are the result of natural optimization through long-term evolution. They possess inherent advantages in terms of drag reduction, mass transfer, and uniform diffusion. Compared to structures like straight channels, flow channels designed with inspiration from these structures exhibit better fluid distribution and mass transfer properties, ensuring a uniform supply of material to all areas while maintaining a low pressure drop, thus improving overall distribution efficiency. Considering that the airflow in a single-orifice thrust bearing structure exhibits the same point-to-area flow characteristics as the liquid transport in a plant leaf, as shown in Figure 1a. The blue arrows in Figure 1, represent the diffusion of the fluid. The biomimetic-compound recess inspired by the branching structure of leaf veins has been designed to enhance the throttling effect of the recess structure and improve its ability to transport air within the bearing air film, thereby enhancing the overall performance of the bearing.
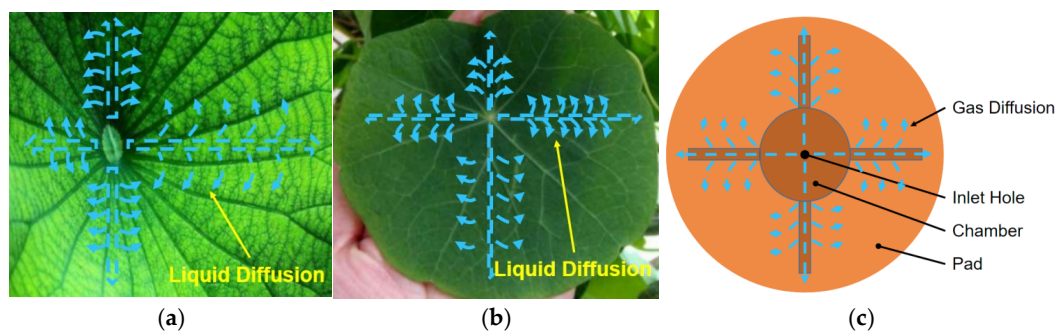

Figure 1. Two similar leaves to single-hole thrust bearings: (**a**) Lotus leaf, (**b**) Nasturtium leaf, (**c**) Schematic diagram of aerostatic bearing.

The branching structure of plant leaf veins, as illustrated in Figure 2, plays a critical role in enabling material exchange and nutrient transport within the leaf. This system ensures the efficient and even distribution of water and nutrients throughout the leaf. The structure is hierarchical, where $k = 1$ and 2 represent the primary and secondary levels, respectively. The hydraulic diameters at each level are $2R_0$ and $2R_1$, with the angle between the levels denoted by θ_1 and the lengths of the main and secondary branches represented by l_1 and l_2. Research indicates that the ratios of these structural parameters at each level significantly influence the hydraulic conductivity of the leaf vein system [25]. Considering the correlation between the structure and function of the leaf blade shown in Figure 1 and the air static-pressure thrust bearing, this paper adopts a bionic approach by introducing the concept of leaf vein branching from Figure 2 into the design of the recess structure, aiming to explore and expand potential pathways for improving the flow performance of air static-pressure bearings. At the same time, considering the requirement of solid balance of bearings at high speeds, recess is designed with a strictly symmetrical branch structure.
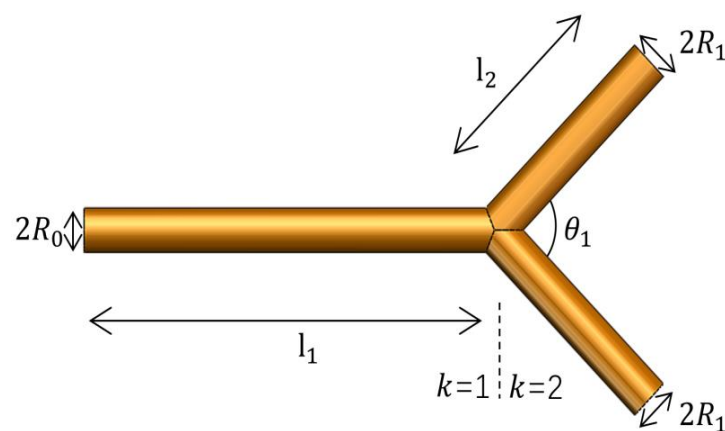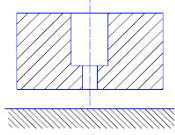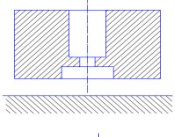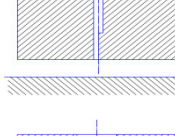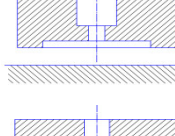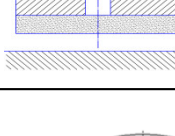

Figure 2. Schematic diagram of bionic branching restrictor structure.

2.2. Physical Models

Aerostatic bearings can be briefly classified into several categories based on the type of recess used. Table 1 [26] illustrates their performance and conducts a longitudinal comparative analysis. Essentially, the bionic-concept recess can be regarded as a variation of simple orifice-type or groove-type recesses. Therefore, to explore the impact of bionic throttle structures on bearing performance, this paper designs three bearings with different recess structures for comparative study. Figure 3 displays the basin diagrams of the bearings with three different recesses, wherein A is the type of bearing with a simple orifice-type recess structure with chambers (SOR); B is the type of bearing with a rectangular-compound recess (RCR); and C is the type of bearing with a bionic-compound recess (BCR). Considering the effects of solid imbalance on bearing operation at high speeds, we have intentionally designed the BCR and RCR structures to be strictly axisymmetric. This design approach ensures uniform mass distribution around the rotational axis, which is essential for maintaining stability and minimizing vibrations at high rotational speeds. The axisymmetric shape facilitates a balanced mass distribution, thereby enhancing the performance and longevity of the bearings in high-speed applications. The three bearings have been designed to maintain the same external diameter D of 40 mm and the same dimensions for the air inlet orifice (diameter D_2 and height H_2). A common range of film thicknesses (from 9 μm to 24 μm) was used. The RCR and BCR have the same pressure-equalizing chamber (diameter D_1 and height H_1) and the same outreach diameter D_0. Meanwhile, we refer to the area within the recess outreach circle as Region I, and the area outside the pure air film section as Region II. In the SOR, we have selected a pressure-equalization chamber with a diameter D_1 ranging from 2 to 30 mm to explore the impact of different chamber sizes on the stability of the bearing. Additionally, within the same range of pressure-equalization chambers, we conduct more comprehensive comparisons of the specific effects of three different structures—A, B, and C—on bearing

performance. This systematic research approach will enhance our understanding of how various design parameters affect the overall performance of the bearing. In comparison with the SOR, the RCR with a rectangular structure is of width L on the outside of the pressure-equalizing chamber, and the height is the same as that of the pressure-equalizing chamber. The BCR, on the other hand, introduces a branching structure on the outside of the pressure-equalizing chamber based on the SOR, creating a compound structural design. For the BCR, the branch structure has a primary slot width of L and a secondary slot width of L_1. Additionally, we define the angle formed by the end of the branching structure and the center of the thrust face as the total angle θ in the BCR, where two secondary slots of the branch structure are equal and symmetrical with respect to the axis centra line and the angle between them is called θ_1. The above designs aim to study the hydrodynamic performance of the bearing by adjusting the recess structure, achieving more rational fluid distribution and more stable air-film support.

Table 1. Comparison of various types of restrictors [26].

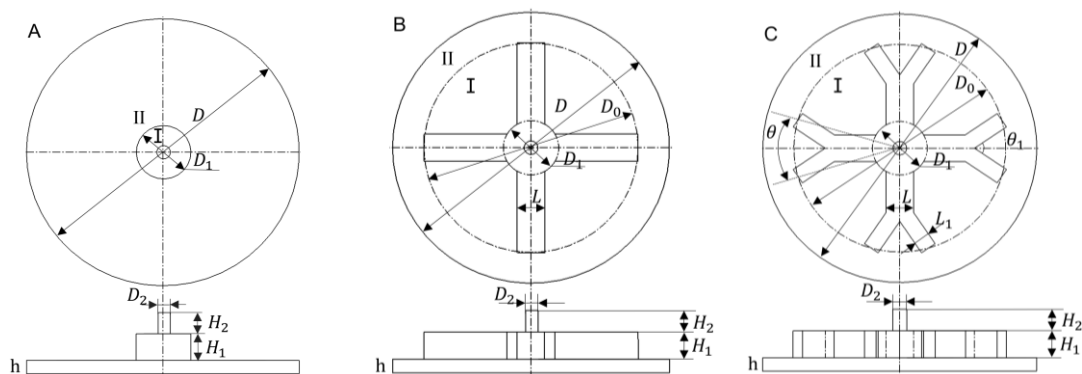| Restrictor Type		Load Capacity	Stiffness	Stability	Air Consumption
Annular orifice		Low	Low	Fair	Small
Simple orifice		High	High	Poor	Small
Slot		Medium	Medium	Good	Large
Groove		High	High	Good	Medium
Porous		High	High	Excellent	Large

Figure 3. Basin diagram of three different recess structures ((**A**): Bearing with SOR structure; (**B**): Bearing with RCR structure; (**C**): Bearing with BCR structure).

To facilitate the subsequent analysis, the entire thrust face was divided into two regions: Region I, which contains the restrict structure, and Region II, which represents the region without a restrict structure. The ratio of diameter D_0 to the external diameter D is recorded as α_i, where the subscript i denotes the item corresponding to different schemes, each with distinct design parameters. It should be noted that, in the designs of the RCR and BCR, when the width of the groove exceeds the diameter D_1 of the pressure-equalizing chamber, the boundary between the chamber and the groove will disappear, causing the compound structure to lose its complexity and ultimately simplify to a groove recess. The parameters of SOR and RCR bearings are shown in Table 2. In designing the parameters of the branching structure, we have drawn on the work of X. D. Shan [27]. According to their conclusions, when the fluid behaves as a laminar flow, the optimal hydraulic diameter ratio R_0/R_1 is 2^(1/3), while in a turbulent flow, this ratio is 2^(7/3). For rectangular cross-section channels, the hydraulic diameter D_h is calculated as follows:

$$D_h = \frac{2WH}{W + H} \tag{1}$$

where W is the width of the rectangular groove structure and H is the height. In this study, according to Equation (1), the width ratios were converted to 0.66 and 0.6, respectively. Since both the simple-orifice and groove recesses are turbulent structures, we chose a width ratio of 0.6 for the BCR to conduct subsequent research.

Table 2. Structure parameters and working conditions.

Calculation Parameters	Value		
	SOR	RCR	BCR
Chamber diameter D_1/(mm)	2~30	2	2
Chamber height H_1/(mm)	1	1	1
Orifice diameter D_2/(mm)	0.2	0.2	0.2
Orifice height H_2/(mm)	0.3	0.3	0.3
Pitch diameter D_0/(mm)	/	20	20
Recess structure ratio α_i	0.05~0.75	0.5	0.5
Primary branch width L/(mm)	/	1	1
Secondary branch width L_1/(mm)	/	/	0.6
Branch angle θ/(°)	/	/	20
Secondary angle θ_1/(°)	/	/	14
Air-film thickness h/(µm)	9~24		
Air temperature T/(K)	293.15		
Density ρ/(kg/m³)	1.202		
Specific Heat c/(J/(kg/m³))	1006.43		
Heat Conductivity k/(W/(m·K))	0.0242		
Viscosity μ/(kg/(m·s))	1.7894×10^{-3}		
Molecular weight m_{mo}/(kg/mol)	28.966×10^{-3}		
Supply pressure P_S/(MPa)	0.5/0.6		
Environmental pressure P_O/(MPa)	1.01325		

3. Numerical Modeling

3.1. Governing Equations

The air within the bearing is considered a compressible viscous fluid, assumed to obey ideal air law. Given the complexity of the flow, this paper employs the full Navier–Stokes equations for numerical simulation [28] to more accurately characterize the air state inside the bearing. The following assumptions are made: the lubricating air is treated as a Newtonian fluid with a constant viscosity coefficient μ; inertial forces are neglected; the pressure and air density between the air films remain constant in the direction perpendicular to the bearing; the y-axis is defined as perpendicular to the air-film surface; and the time-dependent elements can be ignored for steady flow conditions. The equations can be expressed as follows:

Continuity equation:

$$\frac{\partial \rho}{\partial t} + \frac{\partial(\rho u)}{\partial x} + \frac{\partial(\rho v)}{\partial y} + \frac{\partial(\rho w)}{\partial z} = 0 \tag{2}$$

where x, y, z are the coordinates; u, v, w are the velocities in the x, y, z directions; and ρ is the density of the air.

Momentum equation:

$$\frac{\partial(\rho u)}{\partial t} + \text{div}(\rho u \boldsymbol{u}) = -\frac{\partial P}{\partial x} + \text{div}(\mu \text{ grad } u) + S_{Mx} \tag{3}$$

$$\frac{\partial(\rho v)}{\partial t} + \text{div}(\rho v \boldsymbol{u}) = -\frac{\partial P}{\partial y} + \text{div}(\mu \text{ grad } v) + S_{My} \tag{4}$$

$$\frac{\partial(\rho w)}{\partial t} + \text{div}(\rho w \boldsymbol{u}) = -\frac{\partial P}{\partial z} + \text{div}(\mu \text{ grad } w) + S_{Mz} \tag{5}$$

where x, y, z are the coordinates, $\boldsymbol{u}$ is the velocity vector, P is the air pressure, μ is the air kinetic viscosity, and S_{Mx}, S_{My}, S_{Mz} are the momentum sources.

3.2. Computational Domain and Mesh

This study was conducted using CFD simulations with the commercial software ANSYS FLUENT 2022 R1. Given that the thickness of the air film is three orders of magnitude smaller than that of the entire geometry, it is necessary to refine the mesh at the location of the air film to meet the simulation requirements. Meshing the entire geometry, however, would lead to a significant increase in the number of cells. Considering the axisymmetric nature of the flow field in the aerostatic thrust bearing, we employ a quarter model of the entire physical region, as shown in Figure 4a, and apply symmetric boundary conditions for the calculations to minimize computational costs. The model was meshed hexahedrally using ICEM, incorporating 11 mesh layers into the air film, along with refined meshing at critical locations to ensure that the value of y+ remains below 1, as illustrated in Figure 4b. y^+ reflects the resolution of the mesh near the wall, defined by the equation $y^+ = (\rho \tau_W)^{1/2} y / \mu$, where y is the distance from the center of the first layer of the mesh adjacent to the wall to the wall, and τ_W is the wall shear stress. Due to the complexity of the fluid motion in the recess during steady-state calculations, vortex effects resulting from turbulent kinetic energy were observed. Therefore, the RNG (k-e) model was employed to more accurately characterize the vortices within the chamber. The calculations utilized the SIMPLE algorithm for pressure–velocity coupling and second-order upwind interpolation for the density, turbulent kinetic energy, and turbulent dissipation rate, as detailed in Table 2.
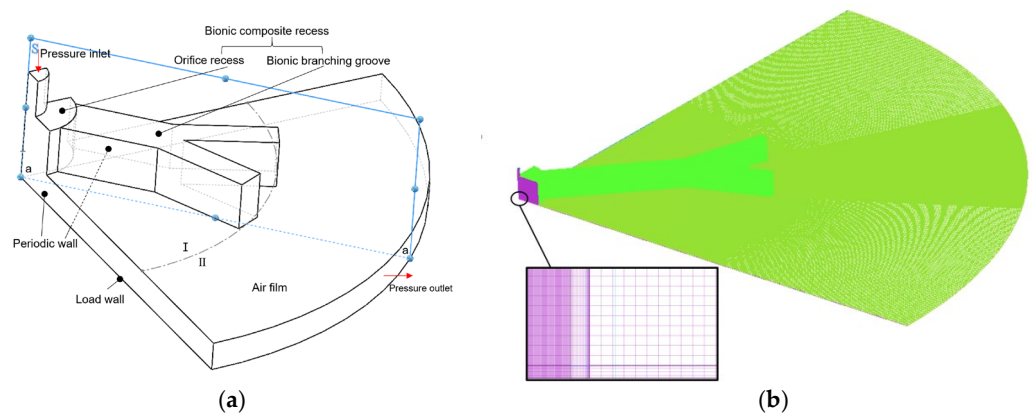

(**a**) (**b**)

Figure 4. Numerical model of the CFD simulations. (**a**) Computational domain and boundary conditions. (**b**) Illustration of computational meshes.

To validate the CFD simulation methodology employed in this study, the results were compared with the experimental findings of Belfort et al. [29]. The circular-chamber simple-orifice recess model from their work was adopted, the simulation was carried out under the same working conditions using our methodology, and the pressure distribution graph shown in Figure 5 was obtained. The simulation results are largely consistent with the experimental data, with an error margin not exceeding 5%, which is acceptable for engineering applications.
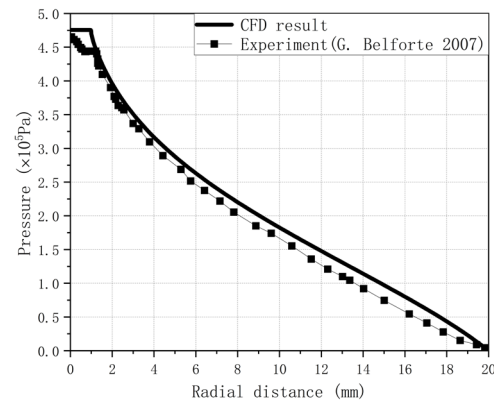

Figure 5. The comparison of radial pressure distribution between CFD result and the existing experimental results [29].

4. Result and Discussion

Qiang Gao et al. [30] demonstrated the pressure distribution in a aerostatic thrust bearing, as illustrated in Figure 6. In the upper diagram of Figure 6, the area outlined by the blue line demonstrates the pressure distribution on the bearing load surface. In the lower diagram in Figure 6, the dark blue area represents the bearing structure, while the light blue area shows the bearing basin. It indicates that for the thrust bearing, when the height of the recess structure significantly exceeds the thickness of the air film, the pressure on the thrust surface within the recess structure (Region I) remains nearly uniform. Conversely, the pressure outside the air outlet (Region II) basically exhibits a linear pressure drop.
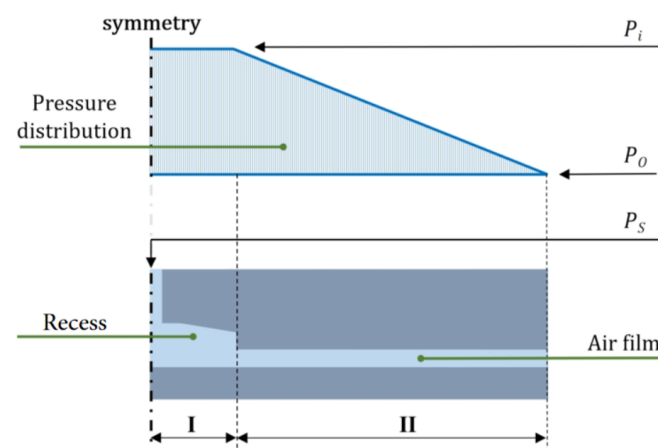

Figure 6. Pressure distribution maps in the aerostatic bearing.

Building on the previous discussion, we can obtain the load-carrying capacity on the thrust surface by individually integrating the pressure over Regions I and II.

$$F_{Ii} = \pi P_i \left(\frac{\alpha_i D}{2}\right)^2 \tag{6}$$

$$F_{IIi} = \int_{\alpha_i L}^{L} 2\pi x (L - x) \frac{P_i}{(1 - \alpha_i)L} dx = \pi \left(\frac{D}{2}\right)^2 P_i \left(\frac{1}{3}(1 + \alpha_i) - \frac{2}{3}\alpha_i^2\right) \qquad (7)$$

$$F_{Ii} + F_{IIi} = F_i = \frac{\pi (D/2)^2 P_i}{3}(1 + \alpha_i + \alpha_i^2) \qquad (8)$$

where D is the bearing disc diameter; α_i is the size ratio of the recess structure to the bearing; F_{Ii} is the force load on thrust surface by air in Region I; F_{IIi} is the force load on thrust surface by air in Region II; and F_I is the total load on the thrust surface combined from Region I and Region II.

According to the equation, it can be concluded that the pressure P_i inside the recess structure in Region I and the percentage of coverage α_i of the recess are both positively correlated with the bearing's capacity. This means that to increase the actual load capacity of the thrust bearing, it is necessary to simultaneously increase the pressure P_i inside the pressure-equalizing chamber and the percentage of coverage α_i of the recess, which is also the expectation for the bionic recess structure in this study. In fact, P_i is a function of α_i, meaning that the pressure within the recess must change according to the design scheme; however, this does not prevent our ability to qualitatively analyze the load capacity in the equation.

Referring to the literature [29], by analogy with Volt's law of transmission, the resistance of Region I and II of the structure is expressed in terms of R_{Ii} and R_{IIi}, using M'_i to represent the mass flow rate, expressing the relationship between the differential pressure and the resistance and flow as follows:

$$M'_i(R_{Ii} + R_{IIi}) = \Delta P = P_S - P_O \qquad (9)$$

where ΔP is the total pressure difference between the air inlet and outlet, and P_S and P_O are pressure defined as the inlet and outlet pressure, as shown in Figure 6. Then, it can be expressed in Region II:

$$M'_i R_{IIi} = \Delta P_{IIi} = P_i - P_O \qquad (10)$$

Putting M'_i in (9) on one side of the equal sign and substituting it into (10), we obtain

$$P_i = P_O + \left(\frac{P_S - P_O}{R_{Ii} + R_{IIi}}\right) R_{IIi} \qquad (11)$$

To enhance the discussion on the impact of flow resistance in each region on the performance of the thrust bearing. Defining the pressure-drop ratio $E = (P_S - P_i)/(P_S - P_O)$, according to Equations (9) and (10), it can be shown that

$$E = \frac{R_{Ii}}{R_{Ii} + R_{IIi}} \qquad (12)$$

Substituting Equation (11) into Equation (10), we obtain

$$P_i = P_O + (P_S - P_O)(1 - E) \qquad (13)$$

It is evident that the pressure P_i in Region I increases as the pressure ratio E decreases (smaller R_{Ii}). According to Equation (8), the ideal design can be summarized as having a large proportion α_i of the recess structure and a low flow resistance R_{Ii} of the recess structure in Region I.

The results from [31] indicate that, although the fluid near the inlet of the recess exhibits turbulent flow, it can still be largely considered a laminar flow due to the size of the air film, and the velocity there was lower than 0.1 Ma. Thus, the air flow in Region II can be characterized as the flow of incompressible air within an expansive annular slit. According to Poiseuille's law, we have

$$V(r) = -\frac{h^2}{12\mu}\frac{dP}{dr} \tag{14}$$

where $V(r)$ is the velocity of fluid in radial coordinate, μ is the viscosity of the fluid as shown in Table 2, and dP/dr is the pressure gradient distributed radially along the thrust surface.

Since the fluid is incompressible, the volume flow Q on the surface of the ring is conserved at any radius r, so that

$$Q = 2\pi h \cdot V(r) \tag{15}$$

Substituting Equation (14) into (15) gives

$$Q = -\frac{\pi h^3 r}{6\mu}\frac{dP}{dr} \tag{16}$$

Organizing Equation (16), the radial pressure gradient of the annular slit is obtained as follows:

$$\frac{dP}{dr} = -\frac{6\mu Q}{\pi h^3 r} \tag{17}$$

In order to obtain the corresponding pressure drop in Region II, integration is performed in the radial $\alpha_i L$ to L region

$$P_i - P_O = \frac{6\mu Q}{\pi h^3}\ln(\frac{1}{\alpha_i}) \tag{18}$$

Substituting the above equation into Equation (10) gives the following structural resistance:

$$R_{IIi} = \frac{6\mu}{\pi h^3}\ln(\frac{1}{\alpha_i}) \tag{19}$$

In Equation (19), R_{IIi} will diminish as α_i increases. According to Equations (12) and (13), we need a design that enables E to decline as α_i grows, indicating that R_{Ii} should decrease more rapidly than R_{IIi}. To verify the effect of α_i on the performance of the aerostatic thrust bearings, the SOR model was first compared with different-sized chamber designs.

4.1. SOR Bearings with Different Recess Ratios

To investigate how the recess structure affects bearing performance, a series of simulations of SOR bearings with different chamber dimensions (size ratio α_i) and air-film thicknesses were conducted and analyzed under the working conditions of P_S = 0.5 MPa.

4.1.1. Load Capacity and Pressure Distribution of SOR Bearings

Figure 7 demonstrates the load capacity of SOR bearings for different values of α_i at different air-film thicknesses. It can be found that, when the selected film thickness is smaller at 9 μm, the overall bearing load capacity increases as the diameter of the chamber increases, though this trend gradually slows down. When the thickness of the air film $h > 12$ μm, the load capacity of the bearings with increasing chamber diameter shows an initial increase and then decreases, and the peak occurs at the diameter of 20 mm (i.e., $\alpha_i = 0.5$). Meanwhile, Figure 7 shows that with the increase in air-film thickness, regardless of the type of SOR, the bearing load capacity exhibits a downward trend, and the differentiation also decreases. When the air-film thickness reaches 24 μm, the bearing load capacity tends to be similar across the board, but it can still be observed that larger α_i values are at a disadvantage. This reflects the interaction between pressure drops and the pressure-holding effect for different α_i values under compromised conditions.
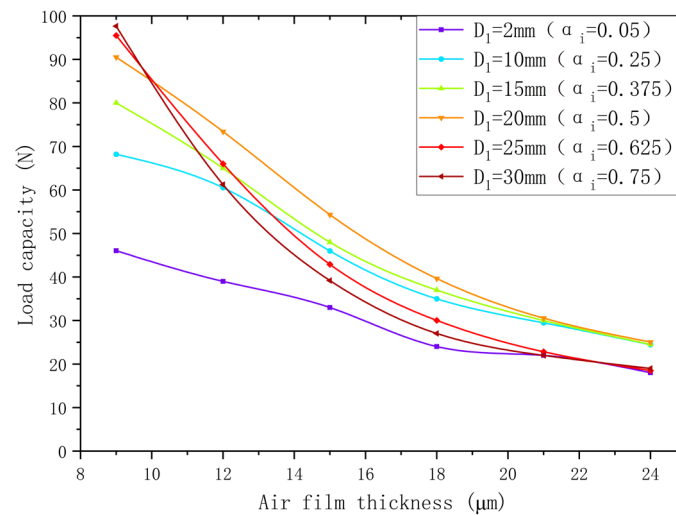
Figure 7. Bearing load capacity for different α_i at different air-film thicknesses.

Pressure distributions in the radial direction of the SOR with varied α_i under the film thickness of 15 μm are shown in Figure 8. It can be observed that the bearing load capacity primarily relies on the pressure-holding effect of the recess structure, which refers to its ability to maintain the diffusion of the central high-pressure region outward, along with the pressure drop occurring at different values of α_i.
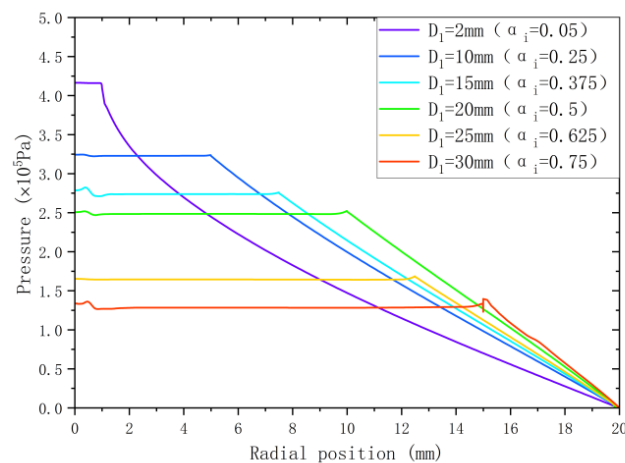

Figure 8. Pressure distribution under different α_i.

Figure 9 shows, from top to bottom, the S-profile velocity streamlines for different α_i values of ROS at $P_S = 0.5$ MPa, $h = 15$ μm. It is observed that, except for the smaller chamber, other schemes exhibit obvious vortex structures downstream of the recess structure. As the air flows out of the chamber into the pure air-film region at the boundary between Region I and II, the drastic change in dimensions leads to a change in the velocity and direction of the flow, resulting in the generation of vortices and the emergence of low-pressure regions. However, the vortex in the small α_i scheme is suppressed by the high pressure near the inlet, while the low-pressure region in the large α_i scheme expands in the opposite direction to the flow. Therefore, despite having a lower structural resistance (flow is not impeded), the SOR scheme fails to achieve an increase in load capacity with increasing α_i. It is judged that there is a limitation of α_i for SOR structures, and thus a balance is needed between lowering structural resistance and limiting the expansion of the vortex at the demarcation to meet the expectations of Equation (8).
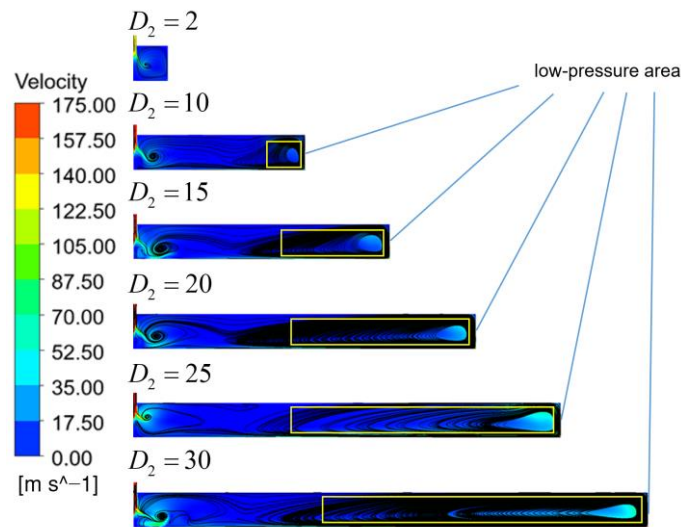
Figure 9. Velocity streamlines at different α_i.

Figure 10 shows the pressure-drop ratios *E* of the SOR under different-sized ratios of α_i. The data show that *E* increases with the enlargement of the recess, i.e., the throttling effect gradually decreases with increasing chamber size. As α_i increases, the bearing pressure-drop ratio of the SOR basically shows a linear growth trend.
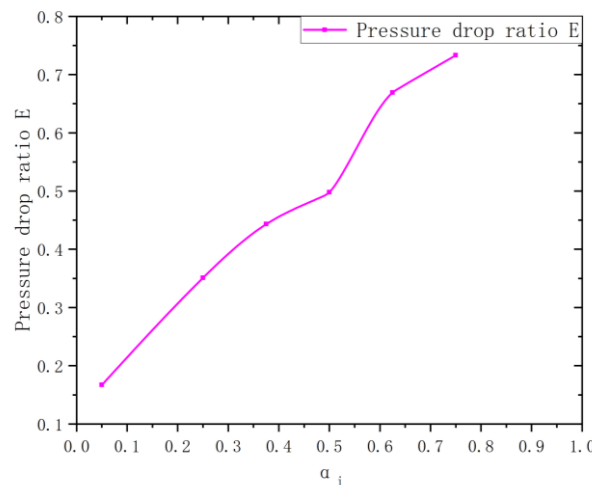

Figure 10. Pressure-drop ratio E with α_i.

4.1.2. Stiffness and Mass Flow Rate of SOR Bearings

Figure 11 shows the stiffness and mass flow rate of different-sized ratios of α_i SOR bearings for different air-film thicknesses. Figure 11a shows that the stiffness of all chambers, except the 25 mm and 30 mm chambers, shows a tendency to increase and then decrease with increasing air-film thickness. The 10 mm, 15 mm, and 20 mm size chambers reach their maximum at an air-film thickness of 12 μm, while the 2 mm chamber reaches its maximum at an air-film thickness of 15 μm. When the air-film thickness $h \leq 12$ μm, the bearing stiffness increases with the increase in the sized ratio α_i. In structures of 25 mm and 30 mm, stiffness decreases rapidly with the air-film thickness, gradually falling below that of the other chamber sizes, and is lower than all structures when the air-film thickness is 21 μm. From the mass flow distribution in Figure 11b, it is evident that the mass flow rate increases with both the air-film thickness and the chamber diameter. Additionally, under different sizes of recess structures, the bearing mass flow rate exhibits varying increases as the air-film thickness rises—the larger the size ratio, the easier it is to reach the critical flow rate as the air-film thickness increases. When the thickness of the air film is 24 μm, the

mass flow rates of different sizes of chambers are basically the same, indicating that the throttling effect is essentially negligible under a large thickness of air film.
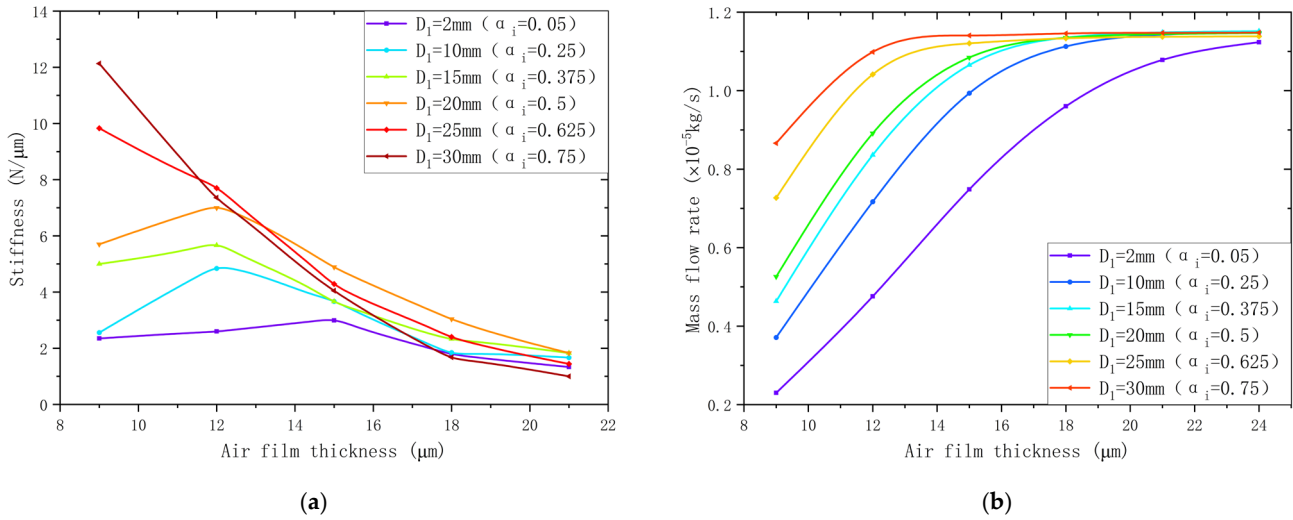

(a)　　　　　　　　　　　　　　　　　(b)

Figure 11. Stiffness and mass flow rate for various α_i: (**a**) Stiffness. (**b**) Mass flow rate.

4.1.3. Dynamic Performance of SOR Bearings

Figure 12 illustrates the velocity contours for different SOR bearings with various sized ratios of α_i, under conditions of $P_S = 0.5$ MPa, $h = 15$ μm. There is only one main vortex present within the chamber. As the chamber diameter increases, the small vortex generated by air separation shifts slightly backward, resulting in the formation of a larger vortex—the larger the chamber, the greater the vortex. According to the research by Xuedong Chen et al. [32], vortices in the chamber are one of the contributing factors to micro-vibrations in bearings. As the intensity of the vortex increases, the associated vibration energy also rises accordingly. Moreover, the pressure drop from the vortex edge to the vortex center directly reflects the intensity of the vortex, which can be used to assess the stability of the bearing. Therefore, in order to more accurately assess the effect of different structures on bearing stability, vector and pressure diagrams of the main vortex positions of different structures were extracted to observe the morphology and pressure distribution of the main vortex. As shown in Figure 12, the main vortex centers of the different structures are at different heights, though all vortices are symmetric with respect to the S-plane (refer to Figure 4). Accordingly, the vector and pressure distributions of each structure at the main vortex position, shown in Figure 13, were extracted along the S-plane. It is clear from Figure 13 that there is a significant pressure drop from the edge of the vortex (where the vortex is no longer clearly visible) to the center of the vortex. The pressure drop generated by the vortex in chambers of different sizes is statistically presented in Table 3. In Figure 13, the behavior of the internal vortex varies under different-sized chambers. When the chamber is small, the pressure fluctuations near the vortex are relatively smooth; however, as the chamber size increases, the pressure fluctuations become more intense. Furthermore, as the chamber enlarges, the vortex also increases in size, and the throttling effect diminishes, causing the high-pressure air at the inlet to directly impact the bottom of the bearing, which poses a potential threat to the stability of the bearing. Additionally, the statistical data in Table 3 regarding the pressure drop by the vortex indicate that the pressure drop in the main vortex region of the bearing tends to increase with the diameter of the chamber. In other words, the intensity of the vortex increases as the chamber section increases. These results demonstrate that an increase in the chamber section affects the stability of the bearing. Therefore, in the SOR structure, a larger chamber volume, represented by the size ratio α_i, results in a less stable bearing.
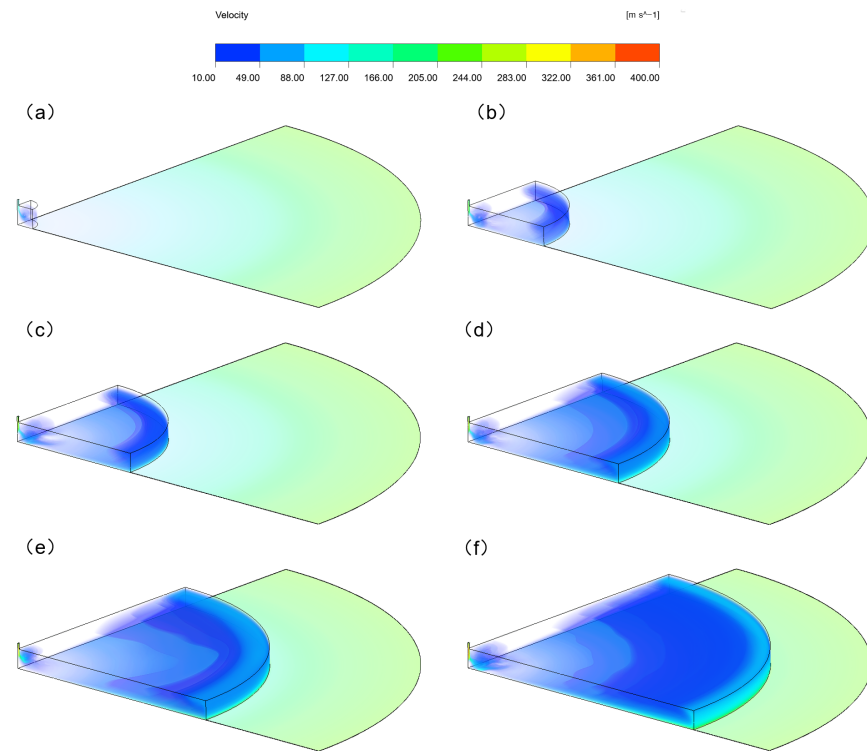
Figure 12. Velocity contours in different-sized chambers. (**a**) D_1 = 2 mm. (**b**) D_1 = 10 mm. (**c**) D_1 = 15 mm. (**d**) D_1 = 20 mm. (**e**) D_1 = 25 mm. (**f**) D_1 = 30 mm.
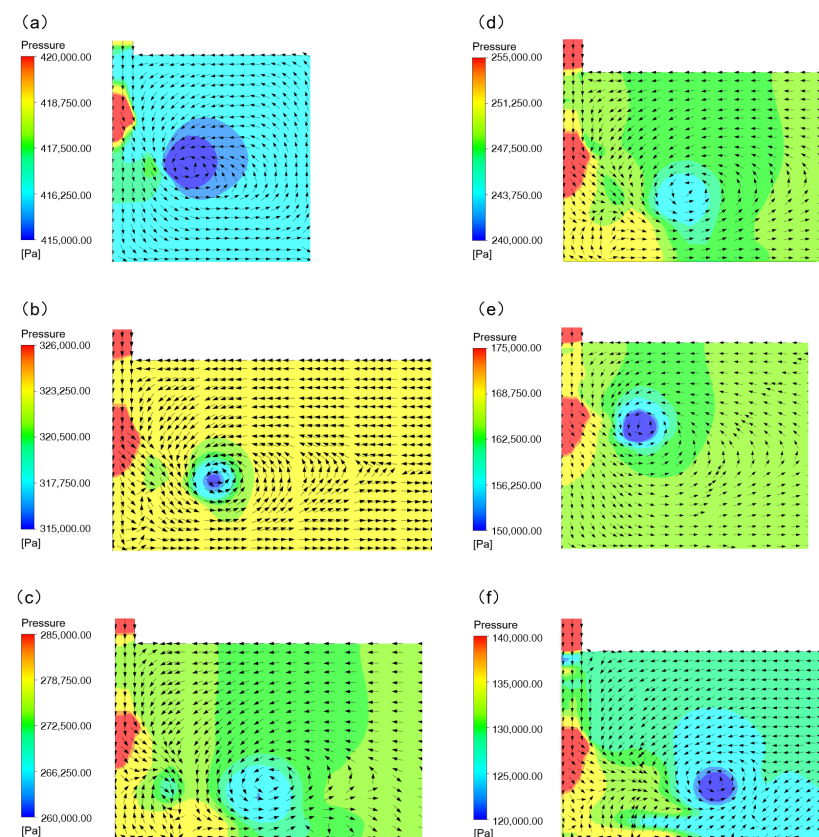

Figure 13. Velocity vector and pressure distribution of different-sized chambers. (**a**) D_1 = 2 mm. (**b**) D_1 = 10 mm. (**c**) D_1 = 15 mm. (**d**) D_1 = 20 mm. (**e**) D_1 = 25 mm. (**f**) D_1 = 30 mm.

Table 3. Pressure drop at different chamber parameters.

Parameters	$D_1 = 2$ mm ($\alpha_i = 0.05$)	$D_1 = 10$ mm ($\alpha_i = 0.25$)	$D_1 = 15$ mm ($\alpha_i = 0.375$)	$D_1 = 20$ mm ($\alpha_i = 0.5$)	$D_1 = 25$ mm ($\alpha_i = 0.625$)	$D_1 = 30$ mm ($\alpha_i = 0.75$)
Pressure drop (Pa)	1250	8023	10,046	15,535	16,028	16,980

In summary, in the SOR structure, the pressure drop and pressure-holding effect caused by the recess are key factors affecting the bearing's load capacity. The ability of the recess to maintain the center pressure is positively correlated with the parameter α_i, while the pressure drop tends to be opposite as α_i increases. Therefore, the key to improving bearing performance is to reduce the ratio of the flow resistance in Region I to that of the entire fluid region as α_i increases. The results indicate that it is crucial to limit the expansion of vortices at the boundary between Region I and II to balance the pressure-holding effect and pressure drop of the recess. Additionally, an increase in α_i enlarges the recess volume, intensifying airflow fluctuations entering the recess structure, which negatively impacts bearing stability. This makes achieving the ideal balance between load capacity and stability more challenging. Therefore, to ensure that the bearing reaches a balance between load capacity and stability, it is necessary to comprehensively consider factors such as the pressure drop caused by the recess structure, the pressure-holding effect and recess volume.

4.2. Effect of Different Recesses on Bearing Performance

The above analyses have been integrated into the design of the RCR and BCR, and the performance of three different types of homogeneous-pressure structure bearings was studied under various working conditions.

4.2.1. Static Performance of Different Types of Recesses

Figure 14 shows the load capacity of various recesses at different air-film thicknesses under a given supply pressure $P_S = 0.6$ MPa, $\alpha_i = 0.5$. It can be observed that the compound recess shows a significant increase in the load capacity compared to the SOR for smaller air-film thickness conditions. This phenomenon suggests that the pressure-holding effect of the recess plays a dominant role in the bearing load capacity in this case. In addition, the BCR commonly has a higher load capacity than the RCR. From the pressure distribution and pressure drop under different structures in Figure 15, it can be seen that although the RCR and BCR are also $\alpha_i = 0.5$, with essentially the same pressure-holding effect, the BCR has a lower pressure-drop ratio, which further results in the load capacity of the BCR exceeding that of the RCR. Figure 15a shows that the main reason for the difference in the pressure-drop ratio is the pressure rise in the branch structure in the sub-stage region, which leads to an increase in the mean pressure and hence a decrease in the pressure-drop ratio. This pressure rise is most likely due to the formation of air accumulation in the sub-stage region as the air flows towards the center on both sides of the branch structure. It is worth noting that the load capacity of all the recesses shows a decreasing trend with increasing air-film thickness. When the air-film thickness is large, there is a significant difference in the variations of pressure drop produced by different recesses, although their pressure-holding effect remains constant. In this case, the pressure-holding effect and the throttle effect balance each other out, so all the results of load capacity tend to be the same.

The pressure-drop ratios of different structures in Figure 15b show that the throttling effect of different types of recesses is roughly divided into three parts, among which the effect of the SOR with a 2 mm chamber is the best, which is much lower than that of other types of bearings. Subsequently, there are SOR bearings and compound recesses with chambers less than 20 mm, and their effect is concentrated in the middle position. Lastly, there are SORs with 25 mm and 30 mm chambers, whose pressure-drop ratio is much higher than that of other types of bearings, and the effect is the worst.
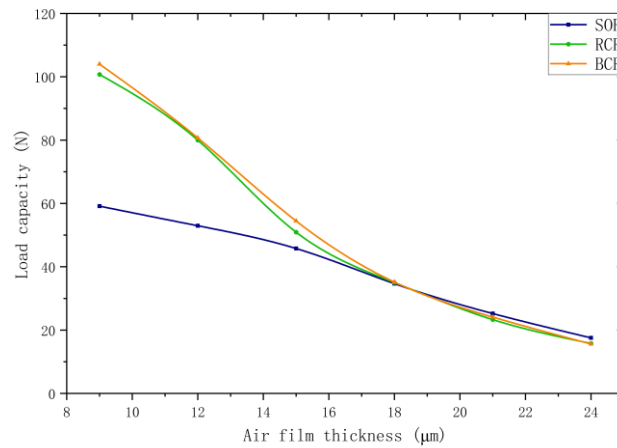
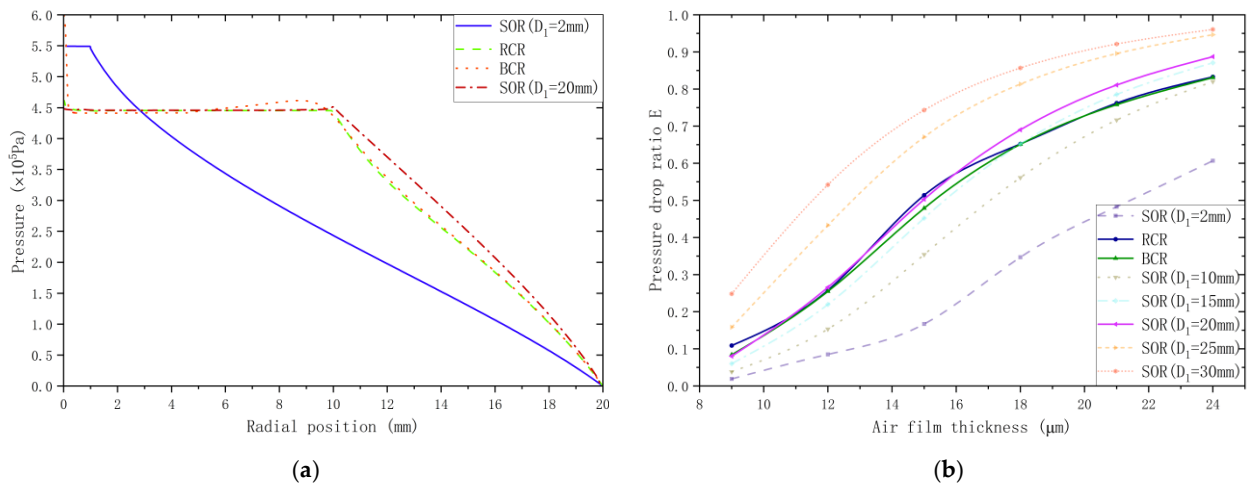**Figure 14.** Load capacity of different recesses at different air-film thicknesses.

(**a**)   (**b**)

Figure 15. Pressure distribution and pressure-drop ratio of different recesses: (**a**) Pressure distributions at $h = 12$ μm. (**b**) Pressure-drop ratios for different recesses at different air-film thicknesses.

When RCR, BCR and SOR bearings have the same α_i, the BCR demonstrates the best throttling effect. Regardless of the film thickness, the BCR's pressure-drop ratio is lower than those of the other two structures. Following this, the RCR only exhibits results lower than for the SOR at smaller film thicknesses. As the film thickness increases, the RCR gradually exceeds the SOR and is essentially the same as the BCR at large thicknesses. In addition, the other two recesses were superior to the SOR. Notably, the throttling performance of these structures decreases as the air-film thickness increases.

Bearing stiffness and mass flow plots for different air-film thicknesses, at a supply pressure $P_S = 0.6$ MPa, of three types of recesses are shown in Figure 16. From Figure 16a, the stiffness of the bearings with different structures exhibits an increasing trend followed by a decrease as the air-film thickness increases. Bearings with compound recesses consistently show greater stiffness than the SOR, indicating that the compound structure at $\alpha_i = 0.5$ enhances bearing stiffness compared to the small-chamber SOR. Additionally, the SOR bearing achieves its highest stiffness at an air-film thickness of 15 μm. while the bearing with a compound recess peaks at 12 μm. The stiffness trends of the RCR and BCR are essentially similar, with the RCR consistently exhibiting lower stiffness than the BCR, regardless of the air-film thickness. When the air-film thickness exceeds 18 μm, the stiffness of all bearing types converges to a similar level.

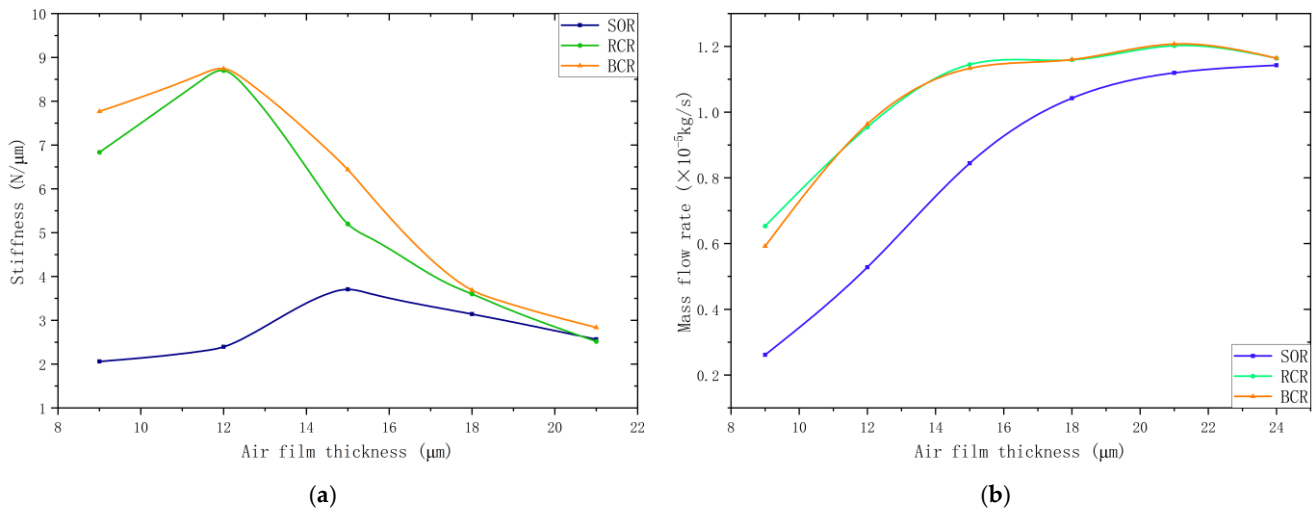**Figure 16.** Stiffness and mass flow rate for different types of recesses: (**a**) Stiffness. (**b**) Mass flow rate.

Figure 16b shows the trend of mass flow rate changes with air-film thickness for different structures. Different structures with increasing air-film thickness are basically the same, showing an increasing trend, and the same trend of the SOR with different chamber sizes is shown in Figure 11, which reaches the critical value at the air-film thickness $h = 24$ μm. The air consumption of the RCR and BCR is roughly equivalent, with the RCR's being slightly higher than the BCR's, and both exceed that of the SOR for small chambers.

4.2.2. Dynamic Performance of Different Types of Recesses

Figure 17 presents the velocity contours for various recess bearings at an air-film thickness of 15 μm and a supply pressure of $P_S = 0.5$ MPa. Just like the small-chamber SOR, the compound recess produces only one main cyclone in the chamber. However, compare to compound recess, the SOR with the same chamber diameter of 20 mm ($\alpha_i = 0.5$) produces a larger cyclone near the inlet by sweeping the small cyclone slightly backwards. Figure 18 shows the main vortex vector diagram and pressure distribution at the inlet of different recesses. The figure indicates that, compared to the small-chamber SOR structure, the compound structure has a weaker throttling effect, and as the chamber volume increases, the vortex in the compound structure becomes larger, resulting in a certain impact from the high-pressure air at the inlet on the thrust surface. However, it can be clearly seen that, compared to the large-chamber SOR structure with the same $\alpha_i = 0.5$, the main vortex of the compound structure is more orderly, the vortex is smaller, and the impact area of the high-pressure air flow on the thrust surface is also smaller. Table 4 shows the pressure drop from the edge to the center of the main vortex inside these bearings. It can be observed that for the same $\alpha_i = 0.5$, the BCR exhibits the smallest pressure drop, followed by the RCR, and finally the SOR. The presence of a secondary branch in the BCR bearing increases the flow path of the air within the throttling structure, and the branch angle impedes the expansion of the low-pressure region at the end of the recess structure toward the air inlet. Therefore, the branch structure not only effectively directs the air but also enhances the stability of the bearing.

Table 4. Pressure drop at different types of recesses.

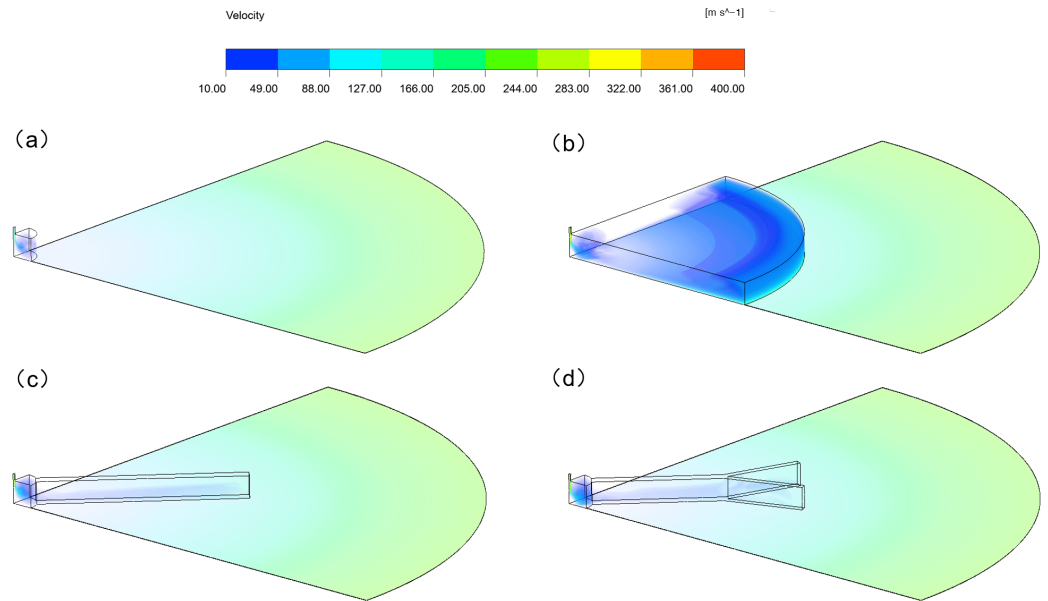| Recess Types (Parameters)	SOC ($D_1 = 2$ mm /$\alpha_i = 0.05$)	SOC ($D_1 = 20$ mm /$\alpha_i = 0.5$)	RCR ($\alpha_i = 0.5$)	BCR ($\alpha_i = 0.5$)
Pressure drop (Pa)	1250	15,535	7961	5470

Figure 17. Velocity contours in different types of recesses. (**a**) SOR with $D_1 = 2$ mm. (**b**) SOR with $D_1 = 20$ mm. (**c**) RCR. (**d**) BCR.
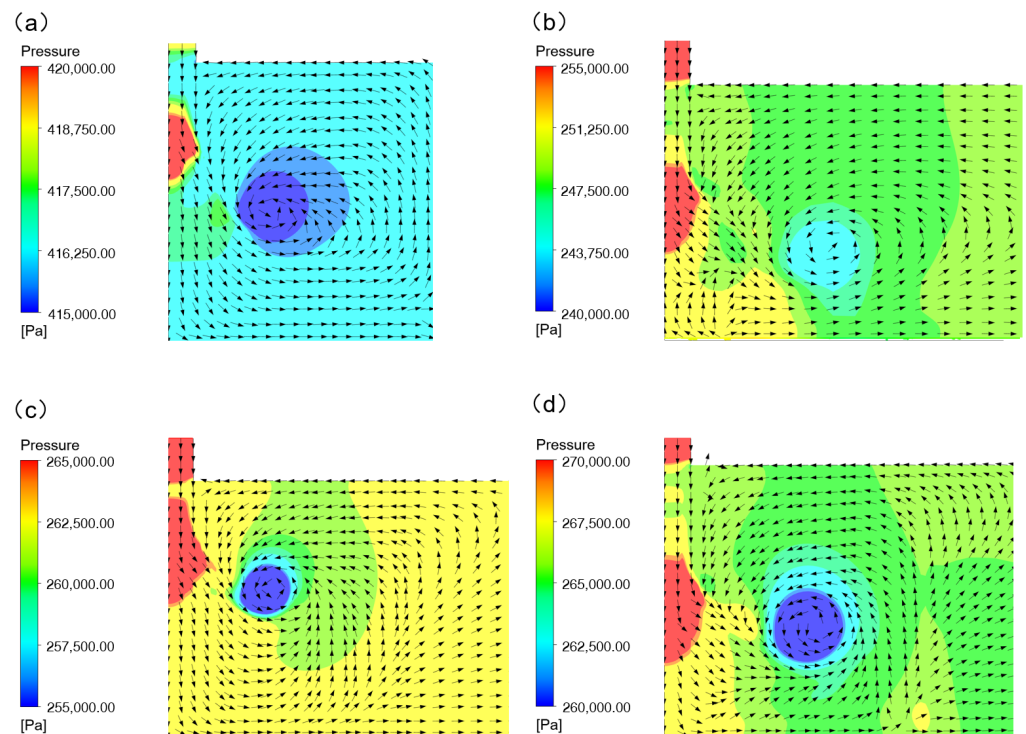
Figure 18. Velocity vector and pressure distribution along the s-plane for different types of recesses. (**a**) SOR with $D_1 = 2$ mm. (**b**) SOR with $D_1 = 20$ mm. (**c**) RCR. (**d**) BCR.

In summary, the compound recess has significant advantages in load capacity and stiffness compared to the small-chamber SOR. Moreover, due to its smaller projected area and air capacity, it also shows significant stability compared to SOR bearings under the same value of α_i. The compound structure not only ensures the pressure-holding distance but also suppresses the expansion of vortices, effectively balancing the bearing's static and dynamic performance. Additionally, thanks to the excellent fluid distribution capability of the bionic structure, the BCR outperforms other structures in both static and dynamic performance.

4.3. Effect of Different Partition Ratios of BCRs on Bearing Performance

The above study found that under the same conditions of α_i, the RCR and BCR achieved significant improvements in stiffness and stability while maintaining similar load capacities, thereby balancing static and dynamic performance. It is noted that the overall performance of the BCR surpasses that of the RCR, which confirms the application potential of bionic structures. To further investigate the effects of the bionic-compound structure on bearing performance, this study varied the proportions of chamber and branch structures in the compound structure while keeping the length ratio, width ratio, and inclusion angle of the branch structure constant. For the sake of convenience in discussion, as shown in Figure 3, we define *CR* as the proportion of the chamber section of the recess structure in Region I as follows:

$$CR = \frac{D_1}{\alpha_i D} \qquad (20)$$

4.3.1. Static Performance BCR Bearings

Figure 19 illustrates the pressure distribution, load capacity, and pressure-drop ratio of BCR bearings with different structural dimensions at a supply pressure of $P_S = 0.5$ MPa and an air-film thickness of $h = 15$ μm. From the pressure distribution graphs of different BCR bearings in Figure 19a, it can be observed that except for the structure where *CR* equals 1 (recess is a chamber without branches), the pressure distribution curves of the other bionic-compound recesses are essentially the same, showing only minor differences at the end. They both exhibit good pressure-holding effects, meaning that the pressure can be maintained after an initial drop until it reaches the 20 mm OD circle. At the same time, the pressure-drop ratio graphs in Figure 19b clearly show the throttling effects of different structures. The *E* value decreases and then increases with an increase in the *CR* ratio, indicating that the throttling effect first increases and then decreases. Obviously, bionic-compound recesses with branch structures outperform those with only chambers in terms of effect. In Figure 19b, it is also shown that the load capacity of different BCR bearings at $h = 15$ μm slightly increases with the increase in the *CR* ratio. By analyzing the top-down pressure field of the thrust surface in Figure 20, the pressure inside the recess remains consistent, while pressure decay occurs outside the recess (in the air film between the branches).
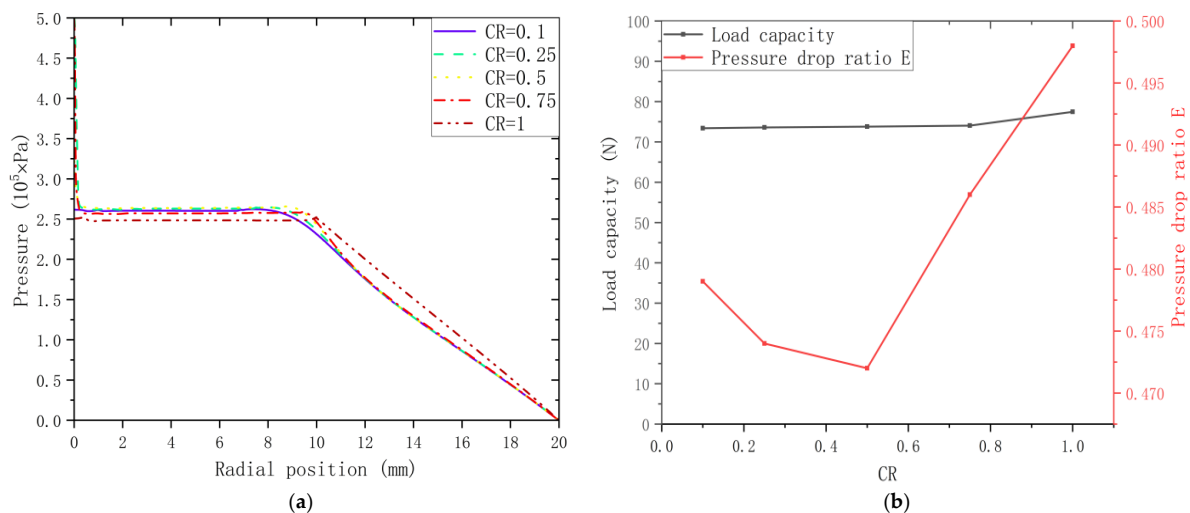

(**a**)   (**b**)

Figure 19. Pressure distribution, pressure-drop ratio and load capacity of bearings with different CR value structures: (**a**) Pressure distribution. (**b**) pressure-drop ratio and load capacity.
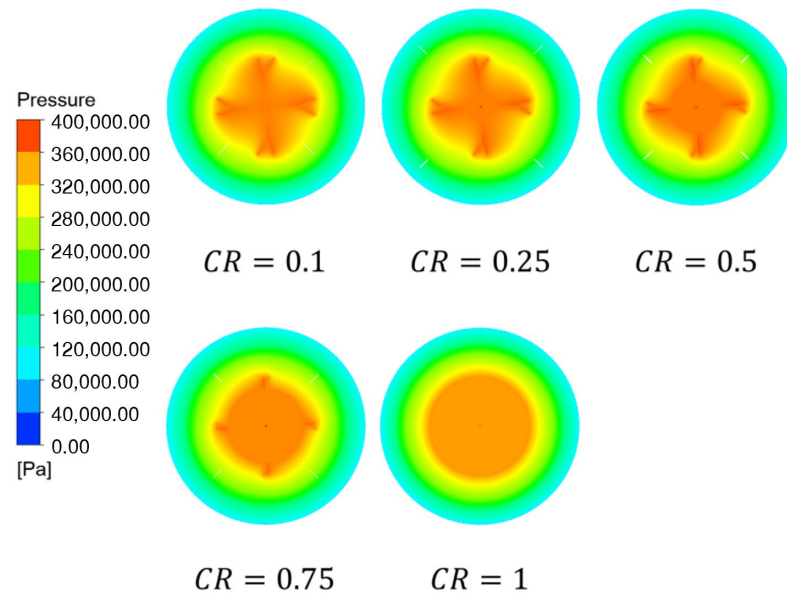
Figure 20. Contours of pressure distribution on bearing surface with different CR values.

4.3.2. Dynamic Performance of BCR Bearings

Figure 21 shows the velocity contours of BCR bearings with different CR ratios under the conditions of P_S = 0.5 MPa and air-film thickness h = 15 μm. Similar to the results of SOC bearings, when the chamber occupies a small proportion of the homogeneous pressure structure, only one main cyclone is generated in the chamber, and then the air diffuses outward through the branch structure. As the chamber section becomes larger, the increased air capacity inside causes the air flowing from the main cyclone at the inlet of the recess to sweep backward, forming a larger cyclone in the chamber. However, this cyclone primarily remains within the chamber, with no obvious vortices in the slot.
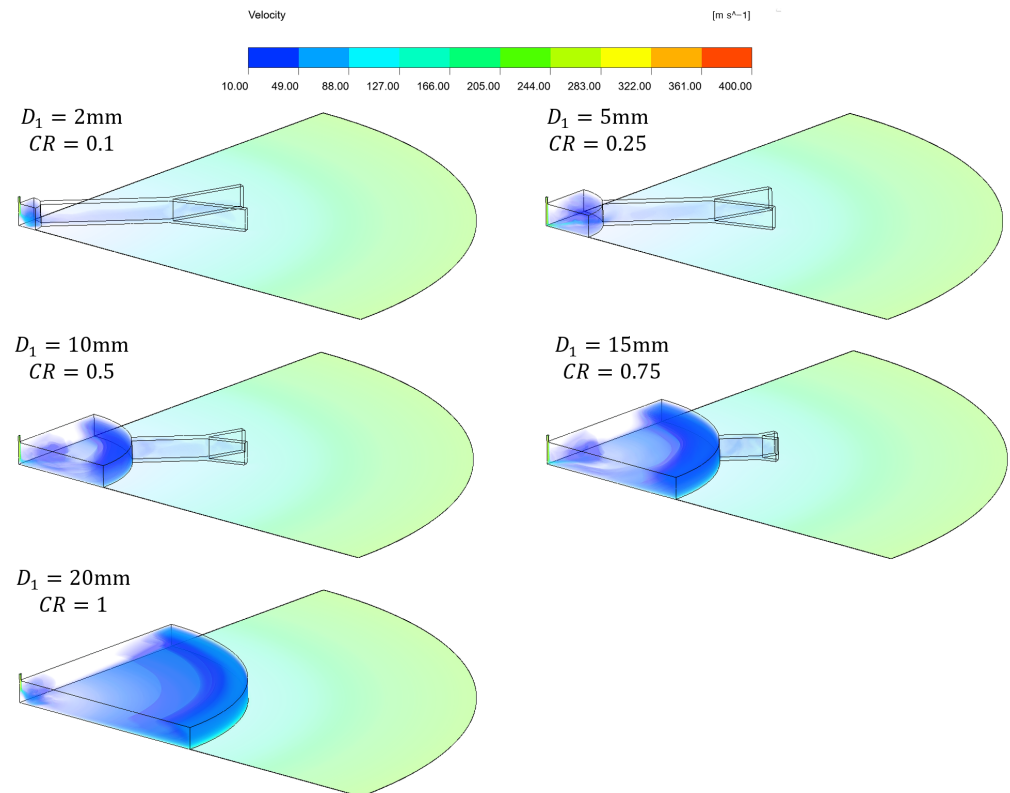

Figure 21. Velocity contours with different CR values.

Figure 22 illustrates the main vortex vector diagram and pressure distribution around the inlet for different CR values. As the CR value increases and the proportion of the chamber section within the recess structure grows, the size of the main vortex at the inlet expands significantly. Additionally, the turbulence intensity within the vortex increases, indicating a more chaotic and irregular airflow pattern. This suggests that as the chamber section grows, the fluid near the inlet becomes more unstable, potentially affecting the pressure distribution and flow behavior, thereby influencing the overall system performance. Meanwhile, Table 5 shows the pressure drop from the edge to the center of the main vortex for different structures. It can be observed that as the void structure increases, the pressure drop tends to rise. This indicates that the proportion of the branch compound structure has a significant impact on the stability of the bearing. As the proportion of the chamber section in the compound recess (i.e., CR) increases, the structural stability gradually declines.
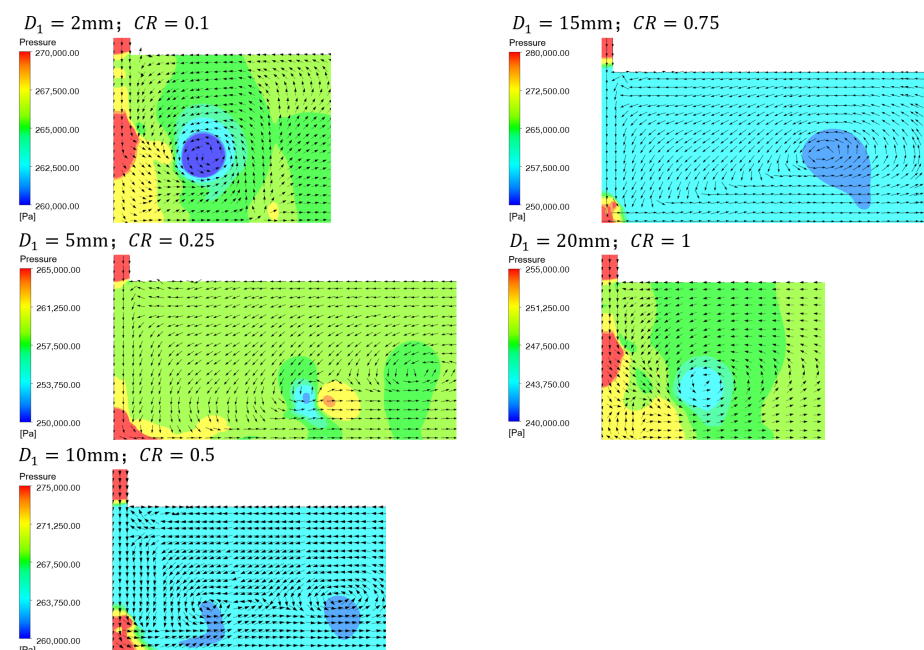

Figure 22. Velocity vector and pressure distribution along the s-plane for different CR values.

Table 5. Pressure drop at different CR values.

Parameters	CR = 0.1	CR = 0.25	CR = 0.5	CR = 0.75	CR = 1
Pressure drop (P_a)	5470	9041	10,623	13,786	15,535

5. Conclusions

This study explores the impact of recess structures on the static and dynamic performance of air static-pressure thrust bearings. Considering the effect of solid imbalance on bearings at high speeds, three structures—SOR, RCR, and BCR—have been designed to strictly adhere to axial symmetry. A series of calculations were conducted through simulation analysis on three representative structures, and the validity of the simulations was verified by comparison with existing experimental data, leading to the following main conclusions:

(1) The throttling effect and pressure-holding effect of the recess are the primary factors determining the static performance of the bearing, and they exhibit opposite trends as the recess's radial ratio α_i changes.

(2) An effective strategy to enhance the bearing's performance is reducing the flow resistance of the recess structure, ensuring that the pressure drop in the throttling region rises slowly, remains stable, or even decreases as α_i increases. This approach strikes an optimal compromise between the pressure-holding effect and the pressure drop.

(3) The compound recess balances both the throttling effect and pressure-holding effect, significantly improving the static performance of the bearing. Moreover, due to its smaller air capacity compared to the traditional simple-chamber recess, it offers a clear advantage in stability, achieving an effective balance between the static and dynamic performance of the bearing.

(4) The BCR equipped with a branch structure has excellent fluid distribution capability. It effectively controls the flow resistance in the recess while ensuring that the recess structures' ratio α_i is sufficiently large. Additionally, the branch structure reduces the impact of sudden changes in the structural dimensions at the boundary between the recess and the air film on the pressure distribution at the air inlet. As a result, it performs exceptionally well in both static and dynamic aspects.

Author Contributions: Conceptualization, F.Y. and H.X.; Data curation, F.Y. and B.C.; Formal analysis, F.Y., H.X., J.Z. and Y.W.; Funding acquisition, H.X. and J.Z.; Investigation, F.Y., H.X., J.Z., B.C. and G.C.; Methodology, F.Y., H.X. and J.Z.; Project administration, F.Y. and H.X.; Resources, H.X. and J.Z.; Software, F.Y., H.X., G.C. and X.Z.; Supervision, H.X., B.C. and G.C.; Validation, F.Y., H.X., J.Z. and B.C.; Visualization, F.Y.; Writing—original draft, F.Y. and B.C.; Writing—review and editing, F.Y., H.X., B.C. and Y.W. All authors have read and agreed to the published version of the manuscript.

Data Availability Statement: Data are contained within the article.

References

1. Yan, R.; Zhang, H. Analysis of the Dynamic Characteristics of Downsized Aerostatic Thrust Bearings with Different Pressure Equalizing Grooves at High or Ultra-High Speed. *Adv. Mech. Eng.* **2021**, *13*, 168781402110180. [CrossRef]
2. Wang, Y.; Wu, H.; Rong, Y. Analysis of Hydrostatic Bearings Based on a Unstructured Meshing Scheme and Turbulence Model. *Machines* **2022**, *10*, 1072. [CrossRef]
3. Sahto, M.P.; Wang, W.; Sanjrani, A.N.; Hao, C.; Shah, S.A. Dynamic Performance of Partially Orifice Porous Aerostatic Thrust Bearing. *Micromachines* **2021**, *12*, 989. [CrossRef] [PubMed]
4. Hashimoto, H.; Ochiai, M.; Namba, T. Optimization of Groove Geometry for Thrust Air Bearing According to Various Objective Functions. *ASME J. Tribol.* **2009**, *131*, 041704. [CrossRef]
5. Yoshimura, T.; Hanafusa, T.; Kitagawa, T.; Hirayama, T.; Matsuoka, T.; Yabe, H. Clarifications of the Mechanism of Nano-Fluctuation of Aerostatic Thrust Bearing with Surface Restriction. *Tribol. Int.* **2012**, *48*, 29–34. [CrossRef]
6. Chen, Y.; Huo, D.; Wang, G.; Zhong, L.; Gong, Z. Modelling and Performance Improvement of an Annular Grooved Thrust Air Bearing. *ILT* **2023**, *75*, 1116–1124. [CrossRef]
7. Colombo, F. Dynamic Characterisation of Rectangular Aerostatic Pads with Multiple Inherent Orifices. *Tribol. Lett.* **2018**, *66*, 133. [CrossRef]
8. Yu, P.; Lu, J.; Luo, Q.; Li, G.; Yin, X. Optimization Design of Aerostatic Bearings with Square Micro-Hole Arrayed Restrictor for the Improvement of Stability: Theoretical Predictions and Experimental Measurements. *Lubricants* **2022**, *10*, 295. [CrossRef]
9. Zhuang, H.; Ding, J.; Chen, P.; Chang, Y.; Zeng, X.; Yang, H.; Liu, X.; Wei, W. Numerical Study on Static and Dynamic Performances of a Double-Pad Annular Inherently Compensated Aerostatic Thrust Bearing. *J. Tribol.* **2019**, *141*, 051701. [CrossRef]
10. Gao, S.; Cheng, K.; Chen, S.; Ding, H.; Fu, H. CFD Based Investigation on Influence of Orifice Chamber Shapes for the Design of Aerostatic Thrust Bearings at Ultra-High Speed Spindles. *Tribol. Int.* **2015**, *92*, 211–221. [CrossRef]
11. Yu, P.; Zuo, T.; Lu, J.; Zhong, M.; Zhang, L. Static and Dynamic Performances of Novel Aerostatic Bearings with Primary and Secondary Orifice Restrictors. *Lubricants* **2023**, *11*, 518. [CrossRef]
12. Qiao, Y.J.; Luo, R.; Shi, K.J. Analysis on the Influence for the Sectional Shape of Compound Pressure-Equalizing Groove to the Supporting and Bearing Characteristics of Precision Aerostatic Bearing. *AMM* **2014**, *494–495*, 598–601. [CrossRef]
13. Eleshaky, M.E. CFD Investigation of Pressure Depressions in Aerostatic Circular Thrust Bearings. *Tribol. Int.* **2009**, *42*, 1108–1117. [CrossRef]
14. Li, W.; Wang, G.; Feng, K.; Zhang, Y.; Wang, P. CFD-Based Investigation and Experimental Study on the Performances of Novel Back-Flow Channel Aerostatic Bearings. *Tribol. Int.* **2022**, *165*, 107319. [CrossRef]
15. Gao, S.; Shang, Y.; Gao, Q.; Lu, L.; Zhu, M.; Sun, Y.; Yu, W. CFD-Based Investigation on Effects of Orifice Length–Diameter Ratio for the Design of Hydrostatic Thrust Bearings. *Appl. Sci.* **2021**, *11*, 959. [CrossRef]

16. Yan, R.; Wang, L.; Wang, S. Investigating the Influences of Pressure-Equalizing Grooves on Characteristics of Aerostatic Bearings Based on CFD. *ILT* **2019**, *71*, 853–860. [CrossRef]
17. Feng, K.; Wang, P.; Zhang, Y.; Hou, W.; Li, W.; Wang, J.; Cui, H. Novel 3-D Printed Aerostatic Bearings for the Improvement of Stability: Theoretical Predictions and Experimental Measurements. *Tribol. Int.* **2021**, *163*, 107149. [CrossRef]
18. Jing, D.; He, L.; Wang, X. Optimization Analysis of Fractal Tree-like Microchannel Network for Electroviscous Flow to Realize Minimum Hydraulic Resistance. *Int. J. Heat Mass Transf.* **2018**, *125*, 749–755. [CrossRef]
19. Zhu, R.; Li, K.; Wang, D.; Fei, J.; Yan Tan, J.; Li, S.; Zhang, J.; Li, H.; Fu, S. Biomimetic Optimized Concept with Murray Networks for Accelerated Solar-Driven Water Evaporation. *Chem. Eng. J.* **2023**, *467*, 143383. [CrossRef]
20. Zhou, G.; Zhou, J.; Huai, X. High Performance Vapor Chamber Enabled by Leaf-Vein-Inspired Wick Structure for High-Power Electronics Cooling. *Appl. Therm. Eng.* **2023**, *230*, 120859. [CrossRef]
21. Chai, S.; Mei, X.; Xie, Y.; Lu, L. Inspired Biomimetic Design for Efficient Fluid Channel Configuration Based on Leaf Vein Structures. *Numer. Heat Transf. Part B Fundam.* **2023**, *1*, 1–14. [CrossRef]
22. Peng, Y.; Liu, W.; Wang, N.; Tian, Y.; Chen, X. A Novel Wick Structure of Vapor Chamber Based on the Fractal Architecture of Leaf Vein. *Int. J. Heat Mass Transf.* **2013**, *63*, 120–133. [CrossRef]
23. Wan, X.; Cao, J.; Yang, X.; Wang, L.; Chen, Y.; Cheng, B. Research on The Flow Field of The Pemfc Bipolar Plate Based on The Tree-Like Fractal Theory. *Fractals* **2023**, *31*, 2340185. [CrossRef]
24. Ma, C.; Sun, Y.; Wu, Y.; Zhang, Q.; Wang, Y.; Ding, G. A Bio-Inspired Fractal Microchannel Heat Sink with Secondary Modified Structure and Sub-Total-Sub Fluid Transmission Mode for High Heat Flux and Energy-Saving Heat Dissipation. *Int. J. Heat Mass Transf.* **2023**, *202*, 123717. [CrossRef]
25. Sack, L.; Scoffoni, C. Leaf Venation: Structure, Function, Development, Evolution, Ecology and Applications in the Past, Present and Future. *New Phytol.* **2013**, *198*, 983–1000. [CrossRef]
26. Zhang, G.; Huang, M.; Chen, G.; Li, J.; Liu, Y.; He, J.; Zheng, Y.; Tang, S.; Cui, H. Design and Optimization of Fluid Lubricated Bearings Operated with Extreme Working Performances—A Comprehensive Review. *Int. J. Extrem. Manuf.* **2024**, *6*, 022010. [CrossRef]
27. Shan, X.D.; Wang, M.; Guo, Z.Y. Geometry Optimization of Self-Similar. *Math. Probl. Eng.* **2011**, *11*, 421526. [CrossRef]
28. Ashgriz, N.; Mostaghimi, J. *An Introduction to Computational Fluid Dynamics*, 2nd ed.; Pearson Education Limited: London, UK, 2007; pp. 30–33.
29. Belforte, G.; Raparelli, T.; Viktorov, V.; Trivella, A. Discharge Coefficients of Orifice-Type Restrictor for Aerostatic Bearings. *Tribol. Int.* **2007**, *40*, 512–521. [CrossRef]
30. Gao, Q.; Chen, W.; Lu, L.; Huo, D.; Cheng, K. Aerostatic Bearings Design and Analysis with the Application to Precision Engineering: State-of-the-Art and Future Perspectives. *Tribol. Int.* **2019**, *135*, 1–17. [CrossRef]
31. Zhou, Y.; Chen, X.; Chen, H. A Hybrid Approach to the Numerical Solution of Air Flow Field in Aerostatic Thrust Bearings. *Tribol. Int.* **2016**, *102*, 444–453. [CrossRef]
32. Chen, X.; Chen, H.; Luo, X.; Ye, Y.; Hu, Y.; Xu, J. Air Vortices and Nano-Vibration of Aerostatic Bearings. *Tribol. Lett.* **2011**, *42*, 179–183. [CrossRef]